

## Modeling the motion and detection of particles in microcantilever sensor cells

K. Y. Manning, N. R. Butt, Abdullah Alodhayb, I. Saika-Voivod, and L. Y. Beaulieu

Citation: *J. Appl. Phys.* **113**, 114501 (2013); doi: 10.1063/1.4795273

View online: <http://dx.doi.org/10.1063/1.4795273>

View Table of Contents: <http://jap.aip.org/resource/1/JAPIAU/v113/i11>

Published by the [American Institute of Physics](#).

---

### Related Articles

Sub-picowatt resolution calorimetry with a bi-material microcantilever sensor  
[Appl. Phys. Lett.](#) **102**, 103112 (2013)

Review article: Fabrication of nanofluidic devices  
[Biomicrofluidics](#) **7**, 026501 (2013)

An active one-particle microrheometer: Incorporating magnetic tweezers to total internal reflection microscopy  
[Rev. Sci. Instrum.](#) **84**, 033702 (2013)

A negative-pressure-driven microfluidic chip for the rapid detection of a bladder cancer biomarker in urine using bead-based enzyme-linked immunosorbent assay  
[Biomicrofluidics](#) **7**, 024103 (2013)

Electrokinetic trapping and surface enhanced Raman scattering detection of biomolecules using optofluidic device integrated with a microneedles array  
[Biomicrofluidics](#) **7**, 014111 (2013)

---

### Additional information on J. Appl. Phys.

Journal Homepage: <http://jap.aip.org/>

Journal Information: [http://jap.aip.org/about/about\\_the\\_journal](http://jap.aip.org/about/about_the_journal)

Top downloads: [http://jap.aip.org/features/most\\_downloaded](http://jap.aip.org/features/most_downloaded)

Information for Authors: <http://jap.aip.org/authors>

## ADVERTISEMENT



**AIPAdvances**

Now Indexed in Thomson Reuters Databases

Explore AIP's open access journal:

- Rapid publication
- Article-level metrics
- Post-publication rating and commenting

## Modeling the motion and detection of particles in microcantilever sensor cells

K. Y. Manning, N. R. Butt, Abdullah Alodhayb, I. Saika-Voivod, and L. Y. Beaulieu<sup>a)</sup>  
*Department of Physics and Physical Oceanography, Memorial University of Newfoundland St. John's,  
 Newfoundland A1E 1C6, Canada*

(Received 26 November 2012; accepted 28 February 2013; published online 15 March 2013)

Consideration of the dynamics of the liquid is often neglected in experiments carried out in flow-through microcantilever sensor cells. Thus, fluid dynamics simulations were performed showing that the geometry of the sensor cell and laminar nature of the flow may result in a highly uneven distribution of particulates throughout the cell, and hence an uneven detection rate at individual cantilevers in a multi-lever setup. Various strategies for diverting flow were tested in order to optimize particle capture rates. Additionally, DNA detection experiments were performed that validated our approximations in treating particle-cantilever interactions and provided a semi-quantitative relationship between simulated particle detection and actual cantilever deflections. The results point out the advantages of flow optimization, the need for calibration of individual cantilevers within a multi-lever cell, and the usefulness of simulation in achieving these goals. © 2013 American Institute of Physics. [<http://dx.doi.org/10.1063/1.4795273>]

### INTRODUCTION

Cantilever sensors are micron-sized beams with one end held fixed and the other end remaining free. Typical dimensions of cantilevers are approximately  $50\ \mu\text{m}$  (wide) by  $350\ \mu\text{m}$  (long) by  $1\ \mu\text{m}$  (thick). The cantilevers are typically made of silicon coated with a thin gold film onto which specific receptive molecules that attract target molecules are deposited. When the target molecules are introduced into the sensor cell, they bind to the receptors on the cantilever causing the latter to bend due to the formation of a surface stress. An optical beam deflection system is used to monitor the deflection of the cantilever by reflecting an optical beam from the free end of the cantilever into a position-sensitive photodetector. Cantilever sensors can be used to perform ultra-sensitive measurements of various physical and chemical phenomena such as changes in temperature, surface stress, antigen-antibody interactions, and DNA hybridization.<sup>1-5</sup> This technology has also been used in applications such as the detection of environmental contaminants, pathogens, and screening of toxic substances.<sup>6,7</sup> Cantilever sensors also have many applications in the field of medicine for performing bioassays, diagnosis, and treatment development.<sup>8-10</sup> Excellent reviews have been published outlining many other applications of cantilever sensors.<sup>11-13</sup>

In a typical application, activated microcantilevers are placed in a small enclosure, herein called the sensor cell, which allows the sensors to be sealed from the environment. The target molecules to be detected are introduced into the sensor cell either in a gaseous form or in solution. The gas or liquid is then forced to either flow over the cantilevers or in a static case the gas or liquid is simply placed into the cell. Once the target molecules are injected into the sensor cell, the deflection of the cantilever(s) is(are) monitored as described above. The deflection of the cantilever provides information

on the presence of the target molecules and, if calibrated, can also provide the concentration of the target particles.<sup>11</sup> Understanding how particles move within the microcantilever sensor cell is imperative to improve the sensitivity and rate of particle detection.<sup>14</sup> In many cases, it is necessary to perform multiple measurements of different targets from a single sample. In such cases, it is imperative to not only know the sensitivity of each active cantilever sensor but to also know the relative sensitivity of each cantilever position within the sensor cell. For this reason, it is important to understand how the particles move within the sensor cell.

The sensor cell used in our laboratory consists of a small enclosure approximately  $1\ \text{cm}^3$  in volume. A schematic representation of the system is shown in Figures 1(a) and 1(b) along with a photograph of the sensor cell (viewed from the top) in Figure 1(d). The sensor cell consists of an input, which allows the solution (or gas) to enter the cell, and an output, allowing the solution (or gas) to exit the cell in flow through experiments. The cell has 8 slots located around its perimeter with each slot capable of holding 1 cantilever sensor probe. In typical flow through experiments, a solution containing the target molecules is forced into the cell at a fluid flow rate of approximately  $0.03\ \text{ml/s}$ . The output of the solution is located within a circular trough surrounding the cantilevers. Initially, it was believed that this design would allow all eight cantilevers in the sensor cell to be exposed to the same concentration of target particles as the trough would induce a radial fluid flow from the center of the cell outwards. Unfortunately, as will be discussed in greater details below, the fluid predominately followed a path of shortest distance from the input to the output exposing all eight cantilevers differently.

In order to better understand the factors that influence the detection rate of target particles by cantilever sensors, a qualitative analysis was performed by simulating the flow of target particles in solution within a sensor cell in order to observe the motion of particles and to study the effects of the

<sup>a)</sup>Author to whom correspondence should be addressed. Electronic mail: lbeaulieu@mun.ca.

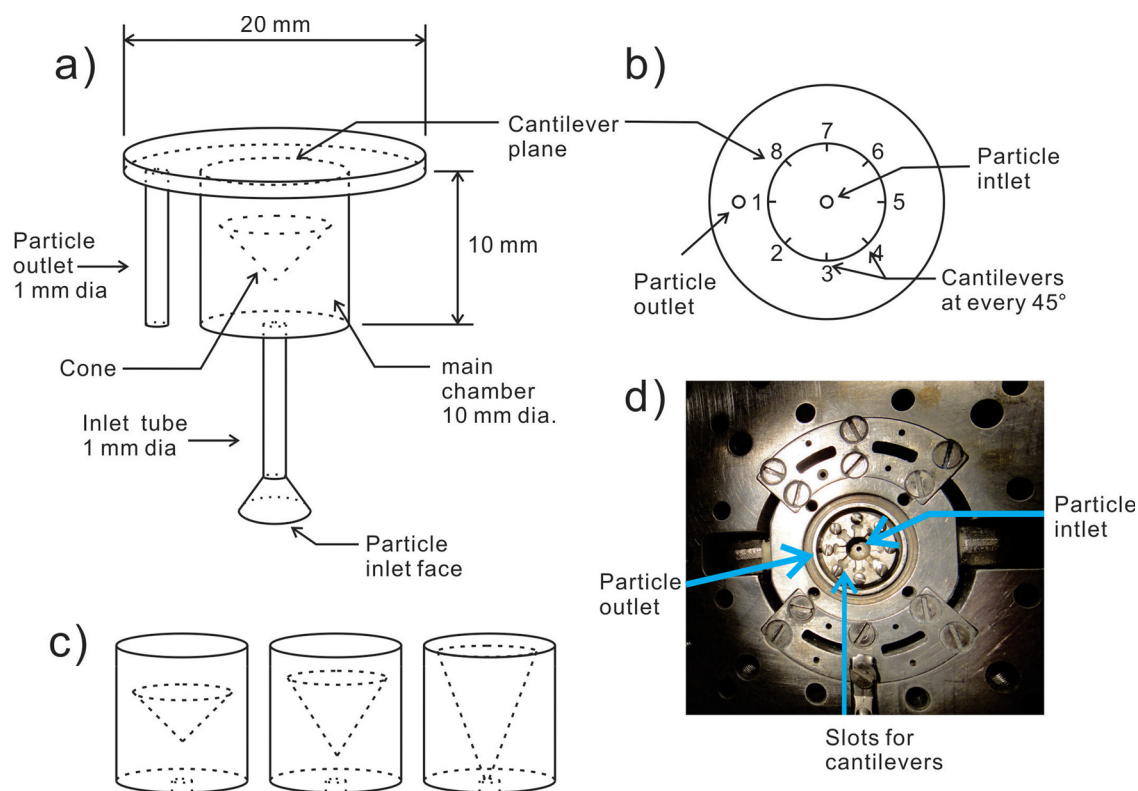


FIG. 1. (a) Schematic representation of the cantilever sensor cell used in our laboratory. (b) Top view of the cantilever plane showing the location of the cantilevers, which have been enlarged to make them visible. Each cantilever is labelled with a number from 1 to 8. Diagram not to scale. (c) From left to right, small, medium, and large inverted cones used in the simulations to force the particles to the edges of the main chamber where the cantilevers are located. (d) Photograph of the sensor cell showing the relative position of the slots that hold the cantilevers, the particle inlet, and the particle outlet.

sensor cell geometry on the detection rate of particles by the cantilevers. It should be made clear that although the current work is presented in the context of cantilever sensing, the application of fluid dynamics calculations plays a significant role in many different types of sensor applications. For example, the fluid cell used to house quartz crystal monitors (QCM) should be designed so as to not interfere with the performance of the crystal, which is already highly damped due to the surrounding fluid. Whether it be in conventional applications or in cases where the crystal has been partitioned to act as a multi-array sensor,<sup>15,16</sup> understanding the fluid flow within the sensor cell is critical for optimizing the sensitivity of the sensor.<sup>17,18</sup> In another application, fluid dynamics calculations are used not so much for optimizing the performance of one sensor but to synchronize two complementary techniques. Surface plasmon resonance (SPR) and QCM are two surface-sensitive characterization techniques, which are complementary each to one another. Since there is no commercial instrument that combines both techniques, the only possible way to perform simultaneous SPR and QCM measurements is to either build your own instrument<sup>19,20</sup> or to determine a method to match the hydrodynamic flow conditions to two separate instruments. Viitala *et al.*<sup>21</sup> used fluid dynamics modeling to determine how to subject two separate instruments to the same hydrodynamics flow conditions so as to improve their ability to study targeted drug delivery systems using two separate commercially available SPR and QCM instruments. In some applications, the biosensor requires a more complex design, which comprises not only

the transducer that interprets the sensing event but also a series of microfluidic channels to introduce several agents, which must be made to first come together to form a reactant before it can be detected by the transducer. In such cases, not only is the delivery of the reactant to the transducer important but also the intermixing of the reagents. In these systems, there are many experimental parameters that affect the performance of the sensor. To perform an analysis on the influence of each parameter experimentally would not only be time consuming but also expensive since many lab-on-a-chip systems require costly micromachining. In this case, performing fluid dynamics simulations is the most feasible alternative to understanding the effect each parameter has on the overall performance of the sensor.<sup>22</sup>

## MODELS

### Computational model

ANSYS<sup>®</sup> FLUENT<sup>™</sup> is a computational fluid dynamics software package used for simulating the motion of fluid in a system. Below, some terms used within FLUENT simulations are given in *italics*. For modeling a small concentration of particles moving within a fluid, the *Discrete Phase Model* was used. This model calculates the trajectories of the particles (discrete phase) using a Lagrangian frame of reference that includes the particles' mass, hydrodynamic drag, and the force of gravity. In this model, the fluid is treated as a continuous phase by solving the Navier-Stokes equations. The discrete phase can be an inert particle, bubble, or droplet.

The motion of the discrete phase is described by equating the particle's inertia with all the forces acting on the particle (shown in the  $y$ -direction)

$$\frac{du_p}{dt} = F_d(u - u_p) + \frac{g(\rho_p - \rho)}{\rho_p} + F_y. \quad (1)$$

Here,  $u_p$  is the particle's velocity,  $u$  is the velocity of the continuous phase,  $\rho_p$  is the mass density of the particle ( $1300 \text{ kg/m}^3$ ),  $\rho$  is the fluid density ( $1000 \text{ kg/m}^3$ ),  $F_y$  is an additional acceleration term that includes Brownian motion and an attraction between the particles and microcantilevers that we describe below,  $F_d$  is the drag force coefficient, and  $g$  is the acceleration due to gravity. The particle density was chosen to be in the vicinity of biomaterials such as DNA or viruses.<sup>23</sup> The drag force is negligible in this case because the velocity of both the particles and the fluid are approximately equal.<sup>24</sup> The continuous phase is governed by the continuity equation and the momentum conservation equations, given as

$$\frac{\partial \rho}{\partial t} + \nabla \cdot (\rho \bar{u}) = 0 \quad (2)$$

and

$$\frac{\partial(\rho \bar{u})}{\partial t} + \nabla \cdot (\rho \bar{u} \bar{u}) = -\nabla p + \nabla \cdot \tau + \rho \bar{g} + \bar{F}, \quad (3)$$

where  $\tau$  is the stress tensor,  $p$  is the pressure and  $F$  is the force exerted by the particles on the fluid, which here is set to zero. In this application, the particles were allowed to interact with the continuous phase and undergo Brownian motion. Two types of simulations were conducted using both the *steady* and *transient* tracking methods. The steady state method solves the time independent flow problem, i.e., by setting time derivatives to zero, while the transient method solves the fully time dependent equations. For well-behaved flows, the two methods should give the same results and so provide a way of checking for consistency. By definition, the steady state simulations provide the unique trajectory traced by a particle entering through a particular position on the velocity inlet face. Particles enter the system using *surface injection*. Each particle was given the same initial velocity. The transient tracking system allows multiple pulses of particles to be injected into the system over time. This type of simulation better displays the bulk motion of the particles, making trends and flow corridors more visible. In this case, particle pulses were injected each second for a total of 30 s.

A *user defined function* (UDF) was developed in order to model the attractive van der Waals forces between the particles and the cantilevers and to record the number of particles trapped by each cantilever. The force between the target particles and the cantilevers was obtained by modifying the van der Waals interaction between two spheres<sup>25</sup>

$$F(D) = \frac{-A}{6} \left\{ \frac{2R_1R_2}{(2R_1 + 2R_2 + D)D} + \frac{2R_1R_2}{(2R_1 + D)(2R_2 + D)} + \ln \frac{(2R_1 + 2R_2 + D)D}{(2R_1 + D)(2R_2 + D)} \right\}, \quad (4)$$

where  $R_1$  and  $R_2$  are the spheres' radii and  $D$  is the distance separating them. To model the cantilever surface, the radius of the second sphere was set to infinity ( $R_2 = \infty$ ) giving the force to be

$$F(D) = \frac{-2AR^3}{3(2R + D)^2D^2}, \quad (5)$$

where  $R$  is the radius of the target particles. The constant  $A$  in Eq. (5) is the nonretarded Hamaker constant based on Dzyaloshinskii, Lifshitz, and Pitaevskii (DLP) theory and is defined by<sup>25</sup>

$$A \cong \frac{3}{4}kT \left( \frac{\epsilon_1 - \epsilon_3}{\epsilon_1 + \epsilon_3} \right) \left( \frac{\epsilon_2 - \epsilon_3}{\epsilon_2 + \epsilon_3} \right), \quad (6)$$

where  $\epsilon_1$  is the dielectric constant of the target particles,  $\epsilon_2$  is the dielectric constant of the fluid, and  $\epsilon_3$  is the dielectric constant of the cantilever surface. Using Eqs. (5) and (6), the force term used in this work was

$$F = \frac{1.698 * 10^{-42}}{(2 * 10^{-7} + D)^2 * D^2}, \quad (7)$$

where the distance  $D$  (m) is measured from the center of the target particle to the base of the cantilever. The force as written above is in units of Newtons.

In the detection of DNA, McKendry *et al.*<sup>26</sup> found that exposing their cantilever sensors to 75 nM solutions of DNA corresponded to a capture of the order of femtomoles of DNA on the cantilever. These numbers indicate that about 0.0000013% (1 in 75 000 000) of the total particles injected into the sensor cell were captured by the cantilever. The simulations performed in this work involved the study of thousands of target particles flowing through the cantilever sensor cell. With such small particle detection numbers, it would have been difficult to observe enough (if any) particle trapping so as to study the effects of cell geometry on the particle detection. In order to compensate for this, the van der Waals force (Eq. (7)) between the particles and the cantilever surface was increased by ten orders of magnitude so as to increase the particle detection rate. It is believed that increasing the van der Waals force allows for qualitative data to be collected however since the increase in the force is the same for each cantilever, the relative ratio of particles detected between different cantilevers should provide a more quantitative description of the influence on the cantilever position within the sensor cell in detecting target particles.

In order for FLUENT to model the motion of particles, the system which houses the fluid must first be created using a graphical user interface to create a 3D representation of the cell that can be imported into the program. In this work, the program GAMBIT<sup>®</sup> was used to create the geometries to describe our system by first creating a volume and then applying a general meshing scheme throughout. Each face was given a boundary condition appropriate to it being an inlet, outlet, or simply a wall. The system used in the simulations, shown schematically in Figures 1(a) and 1(b), was an exact reproduction of the cantilever sensor setup used in our

laboratory (Figure 1(d)). Particles were injected with an initial velocity of 0.01 m/s from the particle inlet face, which corresponds to a particle flow rate of 0.03 ml/s, a typical flow rate used in our experiments. For the steady state, a single injection of 1182 particles was introduced into the cell, whereas for the transient flow simulation, 1182 particles were injected into the cell every second for a total of 30 s. A cone shaped velocity inlet tube, which mimics the syringe used in the experiments, was used to allow more grid faces and consequently more particles to be injected. The solution was injected at the inlet face and traveled up through the inlet cylinder (1 mm dia.) into the main chamber (10 mm dia.) and out through the outlet cylinder (1 mm dia.). The cantilevers are located around the edges at the top of the main chamber called the cantilever plane.

In order to force the target particles to better come into contact with the cantilevers, inverted cones were inserted into the main chamber of the cell, as shown schematically in Figure 1(c). Within the text, these cones will be referred to as small, medium, and large cones in reference to their size. A fourth, more complicated, geometry was used to divert the target molecules to two cantilevers at one time. The flow diverter shown in Figure 2 has a cylindrical geometry with the same outer diameter as the inner diameter of the main chamber. The diverter fits into the main chamber (Figure 2(a)) and allows the solution containing the target molecules to enter the sensor cell and forces it to flow towards two cantilevers (Figure 2(b)) positioned at 90° with respect to the center of the cell. The solution then exits the cell through the particle outlet as in the other cases.

## MATERIALS AND METHODS

Experiments were conducted to investigate the effects of the flow diverter (Figure 2) on the detection of target molecules. Commercially available silicon microcantilevers (MikroMasch CSC12/Tipless microcantilever) 350  $\mu\text{m}$  long, 35  $\mu\text{m}$  wide, and 1  $\mu\text{m}$  thick were used in the experimental portion of this study. Prior to deposition, the microcantilevers were first cleaned with a Piranha solution ( $\text{H}_2\text{SO}_4$ :

$\text{H}_2\text{O}_2 = 3:1$ ) for 5 to 10 min and then washed twice with ethanol and then de-ionized water to remove any residues and contaminations on the surface. After rinsing, the microcantilevers were dried in an oven for 24 h at 275 °C. The cleaned and dried cantilevers were then coated on the top surface with a 20 nm adhesion layer of Inconel followed by a 100 nm thin gold film by sputtering deposition. During all experiments, all active and reference microcantilevers were taken from the same deposition batch to ensure consistency. Reference microcantilevers were used throughout all experiments to eliminate any deflections caused by changes in temperature and/or nonspecific interactions. Microcantilevers used in this study were mounted in a fluid cell where they were exposed to the injected fluids. The fluid cell was attached to two Polyether Ether Ketone (PEEK) tubes used to transport fluid to and from the fluid cell. All fluids used in this study were injected into the fluid cell at a consistent flow rate of 0.03 ml/s, which matches the initial inlet velocity used in our computational simulations.

Deoxyribonucleic acid (DNA) hybridization was used as the reaction mechanism for assessing the impact of the sensor cell geometry on the cantilever detection. Thiolated single stranded (ss) DNA of length 25 bp with a C6 linker (5'-/ThioMC6-D/TCT GTA TGT CAT TGA CAG TCC AGC T-3') purchased from IDT (Integrated DNA Technologies) were immobilized on the surface of the gold coated microcantilevers. An incubation time between 3 and 5 h was found to give the best results although others have found that longer incubation times were preferred.<sup>27</sup>

After immobilizing the probe ssDNA on the microcantilever surface and placing it in the fluid cell, TE buffer was then injected at the flow rate of 0.03 ml/s until the cantilevers came into equilibrium. TE buffer is often used to stabilize the DNA molecules and protects them from degradation.<sup>28</sup> This process also removes physisorbed oligos from the microcantilever surface. Once equilibrium was obtained, a solution containing complementary target ssDNA was injected. The target ssDNA sequence used in this study had the following sequence 5'-AGC TGG ACT GTC AAT GAC ATA CAG A-3'.

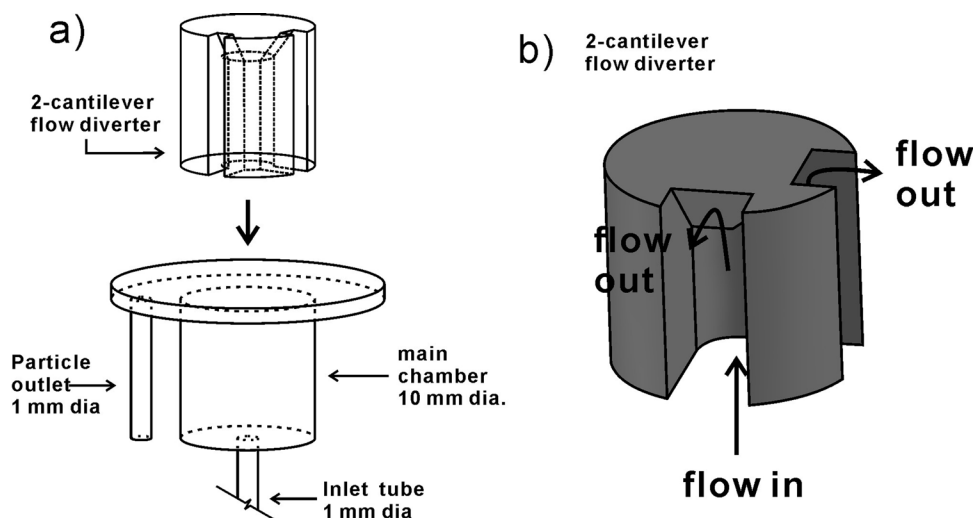


FIG. 2. Schematic representation of the flow diverter used to force the input solution to flow directly over two separate cantilevers. (a) The flow diverter is made to fit in the main chamber of the sensor cell. (b) The fluid enters the cell and is separated into two currents.

## RESULTS

The general properties of the fluid flow in the sensor cell are described by two dimensionless quantities. The Péclet number is a measure of the relative importance of advection to diffusion in a system. For a Péclet number  $P_e \ll 1$ , the fluid flow is dominated by diffusion. In the case where  $P_e \gg 1$ , the fluid flow is dominated by advection. The Péclet number is defined as

$$\frac{\text{diffusive time}}{\text{convective time}} \sim \frac{Q}{DW} \equiv P_e, \quad (8)$$

where  $D$  is the diffusivity of the fluid ( $\sim 10^{-5} \text{ cm}^2/\text{s}$  for water),  $W$  is the width of the cell (1 cm), and  $Q$  is the flow rate (0.03 ml/s).<sup>29</sup> Given the order of magnitude of these quantities for our system, we obtain  $P_e \sim 3000$ , indicating that diffusion of particles is unimportant. Hence, the particles do not tend to randomly diffuse throughout the volume, but rather move along with the fluid. The second dimensionless number that describes the relative importance of inertial and viscous forces is the Reynolds number given by

$$\frac{\rho UL}{\eta} \equiv Re, \quad (9)$$

where  $\rho$  is the density of the fluid ( $1 \text{ g/cm}^3$ ),  $U$  is the velocity of the fluid (1 cm/s),  $L$  is the typical length scale of the system (1 cm), and  $\eta$  is the dynamic viscosity of the fluid at

room temperature ( $0.01003 \text{ g/(cm s)}$ ).<sup>29</sup> We estimate the Reynolds number to be  $Re \sim 100$ , which implies that viscous forces dominate over inertial forces and that the fluid flow will be laminar.<sup>30</sup> As a result of this, the fluid motion can in principle be described using a linear form of the Navier-Stokes equations.<sup>24</sup>

The flow patterns of the particles were very smooth and showed little if any sign of randomness. Time-lapsed animations of the simulations showed that the particle trajectories, as calculated by FLUENT, followed clear paths from the inlet of the main chamber almost directly to the outlet with the fastest particles moving along the most direct path between the inlet and the outlet. By observing time-lapsed animations of the particles, it was found that the fastest moving particles intercepted the cantilever plane near the centre, away from the cantilevers, with a second surge of slower moving particles moving towards the edge closest to the outlet. The fastest moving particles exited the cell, quickly followed by the slower particles.

Figures 3(a)–3(c) show scatter plots illustrating the position of the particles at different time intervals as they move through the sensor cell. The pink spheres indicate the particles as they first enter the cell through the inlet tube. The blue spheres show the particles at some later time as they are 17% up the main chamber (see Figure 1(a) of the sensor cell). The red spheres show the particles at a later time as they are approximately 58% up the main chamber while finally the green spheres show the position of the particles in

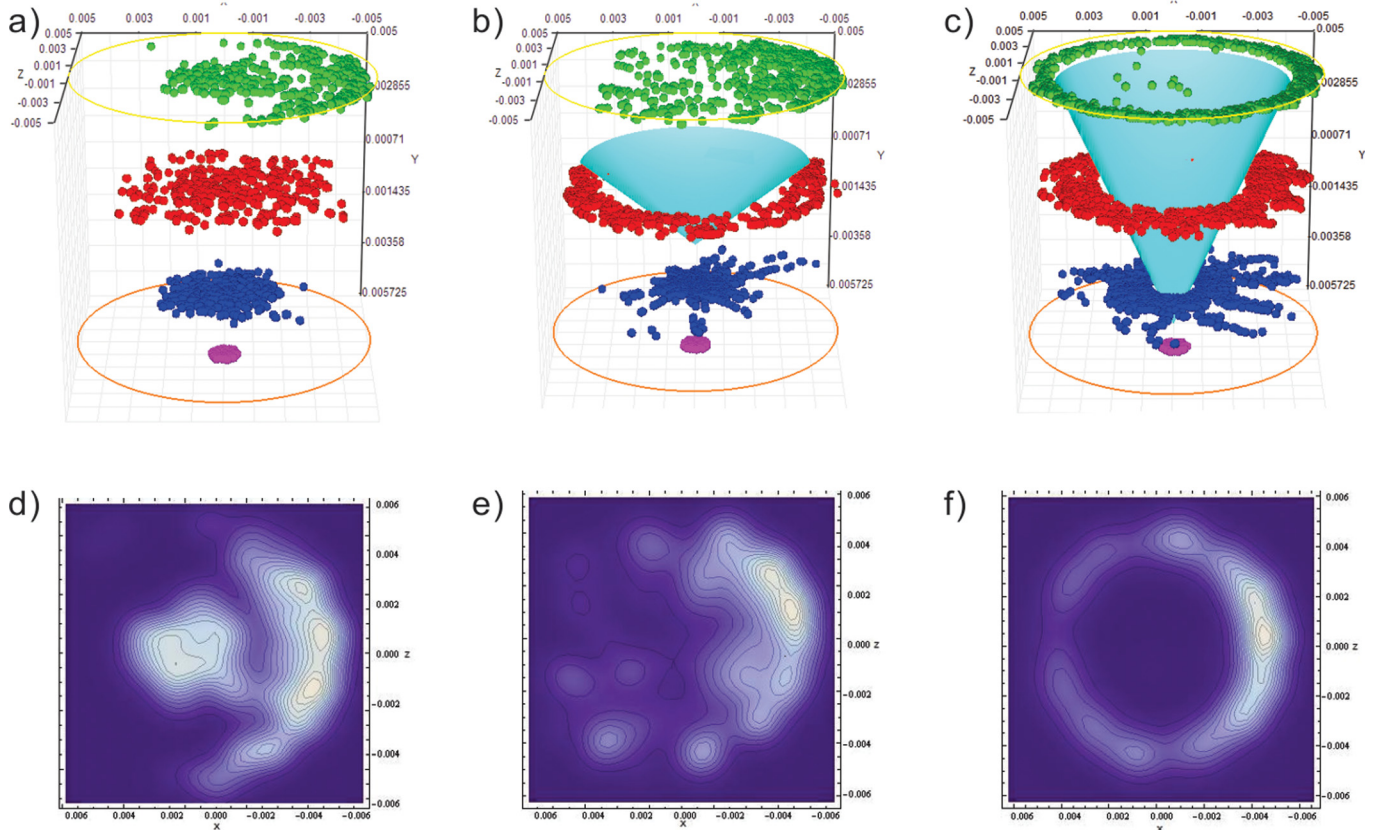


FIG. 3. The time evolution of the particles as they intersect three defined planes within the main cylinder of the (a) original geometry, (b) the small cone geometry (of height 3.3 mm), (c) of the large cone geometry (of height 9.6 mm). Contour plot of the particles intersecting with the cantilever plane for the (d) original geometry, (e) small cone, and (f) large cone.

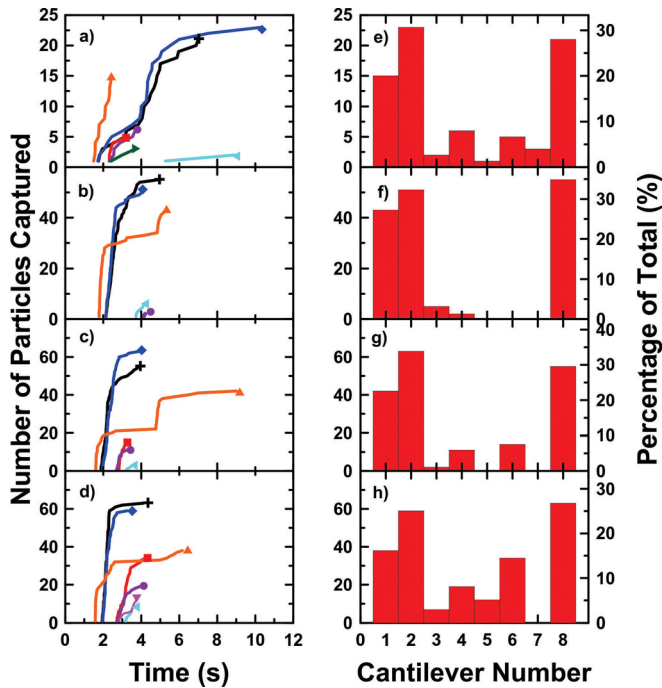


FIG. 4. (a)–(d) Number of particles captured as a function of time for each cantilever for the original geometry (a), small cone (b), medium cone (c), and the large cone (d). Each cantilever is displayed using a different color and symbol: cantilever 1 (orange  $\blacktriangle$ ), cantilever 2 (blue  $\blacklozenge$ ), cantilever 3 (cyan  $\blacktriangleleft$ ), cantilever 4 (purple  $\bullet$ ), cantilever 5 (pink  $\blacktriangledown$ ), cantilever 6 (red  $\blacksquare$ ), cantilever 7 (green  $\blacktriangleright$ ), and cantilever 8 (black  $\blackplus$ ). (e)–(h) Histograms of the total number of particles trapped by each cantilever for the original geometry (e), small cone (f), medium cone (g), and the large cone (h).

the cantilever plane of the sensor cell. In this figure, the yellow circles indicate the bottom and top of the main chamber of the sensor cell with the inlet located at the bottom of the cell and the outlet (not shown) located on the right hand side. Figure 3(d) is a contour plot showing the location of all the particles as they pass through the cantilever plane. This plot clearly shows how only a fraction of the particles come in contact with the cantilevers along the perimeter of the cantilever plane. This central flow behaviour is not ideal for our purpose because most of the particles exit the sensor cell undetected. To eliminate this central flow, inverted cones were placed in the main cylinder of the cell in the hopes of redirecting the particles towards the cantilevers.

Figure 3(b) shows a scatter plot illustrating the effect of a small inverted cone located centrally within the main chamber of the sensor cell. As can be seen the particles enter the sensor cell centrally and are allowed to rise momentarily until they are forced to spread through contact with the cone. As the particles move beyond the top of the cone, they begin to move towards the outlet (on the right, not shown) increasing the dispersion of the particles in the cantilever plane as shown in the contour plot in Figure 3(e). However, as shown in Figure 3(c), the large-sized cone produces a greater dispersion with the particles intercepting the cantilever plane around the perimeter. Although the results are better than the previous two cases, the distribution of particles along the perimeter (see Figure 3(f)) is still not perfectly uniform with a large number of particles gathering at the portion of the cantilever plane closest to the particle outlet.

Figures 3(a) to 3(f) provide a general understanding of how particles move within the cantilever sensor cell with and without the presence of the cones. From these data, we can hypothesize that the large cone geometry should best direct particles towards the microcantilevers located around the perimeter of the cantilever plane. To quantify these results, we investigated the total number of particles trapped by each cantilever as a function of time.

Two types of simulations were conducted to study the detection of target particles by the cantilevers. In the steady case, 1182 particles flowed through the sensor cell, with each particle having an initial velocity of 0.01 m/s at the inlet. As the particles flow through the sensor cell, some interact through the van der Waals force and become trapped by the cantilevers. The cantilevers are labelled from 1 to 8 as shown in Figure 1. Figure 4(a) shows the number of particles trapped on all 8 cantilevers as a function of time as they flow unobstructed (no cone) through the sensor cell. Figure 4(e) shows a histogram of the total number of particles captured by each cantilever (left ordinate) along with the relative percentage of particles detected by each cantilever indicated by the right ordinate. As can be seen, the number of particles detected is highly dependent on the position of the cantilevers with respect to the particle outlet. In this case, cantilevers 1, 2, and 8 captured 78% of all the particles detected (59 out of a total 76 particles captured). Although introducing the cones into the sensor cell increases the total number of particles detected (see Figures 4(b)–4(d) and 4(f)–4(h)), the cantilevers away from the particle outlet still only detected a small fraction of particles compared to cantilevers 1, 2, and 8. Cantilevers 3–7 detected 22% of the total number of particles captured for the case of no cone, 5% using the small cone, 14% using the medium cone, and 31% using the large cone.

One of the effects of the cones is to increase the rate at which particles are detected. Calculating the total number of particles collected by all eight cantilevers as a function of time for each cell geometry shows that the larger cone and the medium cone reached their saturation point (maximum number of particles counted) in less than half the time (44% faster) and two thirds the time, respectively, than the original geometry. In addition, the geometry with the large cone detected approximately 300% more particles than the unmodified cell, 150% more than the small cone, and 125% more than the medium cone. From these results, it is clear that the presence of the cones not only increases the total number of particles detected but also the rate at which particles are detected.

Because steady state simulations provided only one set of particle tracks, it is difficult to establish any trend in the detection patterns since some cantilevers only captured a few particles. For this reason, the transient particle tracking scheme was used to inject a pulse of 1182 particles into the sensor cell through the velocity inlet every second for thirty seconds. Following the initial 30 s, the sensor cell was continued to be monitored with no further injections for ten seconds.

The number of particles trapped on all eight cantilevers as a function of time is shown in Figures 5(a)–5(d) with the

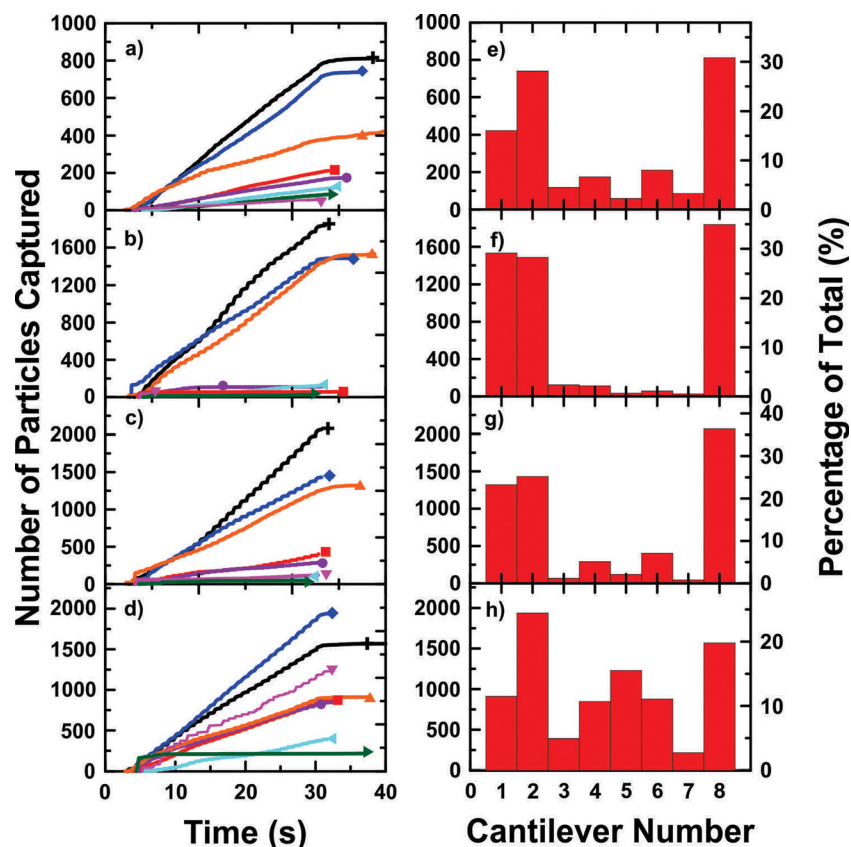


FIG. 5. (a)–(d) Number of particles captured as a function of time for each cantilever for the original geometry (a), small cone (b), medium cone (c), and the large cone (d). Each cantilever is displayed using a different color and symbol: cantilever 1 (orange  $\blacktriangle$ ), cantilever 2 (blue  $\blacklozenge$ ), cantilever 3 (cyan  $\blacktriangleleft$ ), cantilever 4 (purple  $\bullet$ ), cantilever 5 (pink  $\blacktriangledown$ ), cantilever 6 (red  $\blacksquare$ ), cantilever 7 (green  $\blacktriangleright$ ), and cantilever 8 (black  $\blackplus$ ). e–h) Histograms of the total number of particles trapped by each cantilever for the original geometry (e), small cone (f), medium cone (g), and the large cone (h).

total number of particles captured shown by the histograms in Figures 5(e)–5(h). The right ordinates in Figures 5(e)–5(h) show the relative percentage of particles captured by each cantilever. The step-like nature of the data in Figures 5(a)–5(d) is a result of the pulses used to inject particles into the sensor cell. As in the steady case, the cantilevers closest to the particle outlet captured the largest number of particles. In fact, cantilevers 3–7 captured 25% for the geometry with no cone, 7% for the small cone, 16% for the medium cone, and 45% for the large cone. These values are all slightly larger than those observed for the same geometry using the steady state particles injection method. Also, for the large cone geometry, cantilevers 3–7 were found to capture more particles. As in the previous case, not only did the total number of particles captured increase with the size of the cone, but so did the capture rate. This effect is clearly due to the clearer path the particles take towards the cantilevers in the presence of the cones.

Simulations were performed with the two-cantilever flow divider positioned in the cell. In these simulations, 750 particles were injected into the cell every second for 30 s. Figure 6(a) shows the number of particles captured for cantilevers positioned in slots 2 (blue  $\blacklozenge$ ) and 8 (green  $\blacktriangle$ ) without the presence of the two-cantilever fixture. Since there were fewer particles inserted into the cell, the number of particles detected by each cantilever was smaller than as shown in Figure 5. Using the two-cantilever fixture increased the number of particles detected by the cantilevers positioned in slots 2 (purple  $\bullet$ ) and 8 (orange  $\blacksquare$ ) by a factor of approximately 4. When the cantilevers were positioned in slots 4 and 6, the effects were even more dramatic. Figure 6(b) shows the number of

particles detected by cantilevers 4 (blue  $\blacklozenge$ ) and 6 (green  $\blacktriangle$ ) were approximately 60 and 40, respectively. However, when the fixture was inserted the number of particles detected by the cantilevers positioned in slots 4 (purple  $\bullet$ ) and 6 (orange  $\blacksquare$ ) increased to just less than 400. More interesting is that irrespective of where the cantilevers were located, the total number of particles detected was approximately the same as shown in Figure 6(c) where the total number of particles collected when the cantilevers were in positions 2 and 8 (purple  $\bullet$ ) was approximately 800 while the total number of particles collected with the cantilevers located at positions 4 and 6 (orange  $\blacksquare$ ) was approximately 780.

Experiments were also conducted to verify the effects of the two-cantilever flow diverting fixture. Figure 7 shows the results of DNA hybridization experiments for cantilevers positioned in slots 4 and 6 in the sensor cell. In this case however one cantilever was used as a reference cantilever while the second was used as the active cantilever. The black curve shows the cantilever deflection versus time as the cantilevers were exposed to a  $0.5 \mu\text{M}$  solution of ssDNA. As the ssDNA hybridized with the complementary ssDNA immobilized on the surface of the cantilever, a compressive surface stress was generated causing the cantilever to deflect downwards. Because slots 4 and 6 are opposite from the fluid output, the cantilever deflections are small even with a high target concentration. The red curve in Figure 7 shows the cantilever deflection when the active cantilever was exposed to the same target solution of ssDNA with the two-cantilever flow diverter inserted into the cell. As can be seen, the cantilever deflection in this case is approximately 4 times larger than the cantilever deflection observed without the use of the

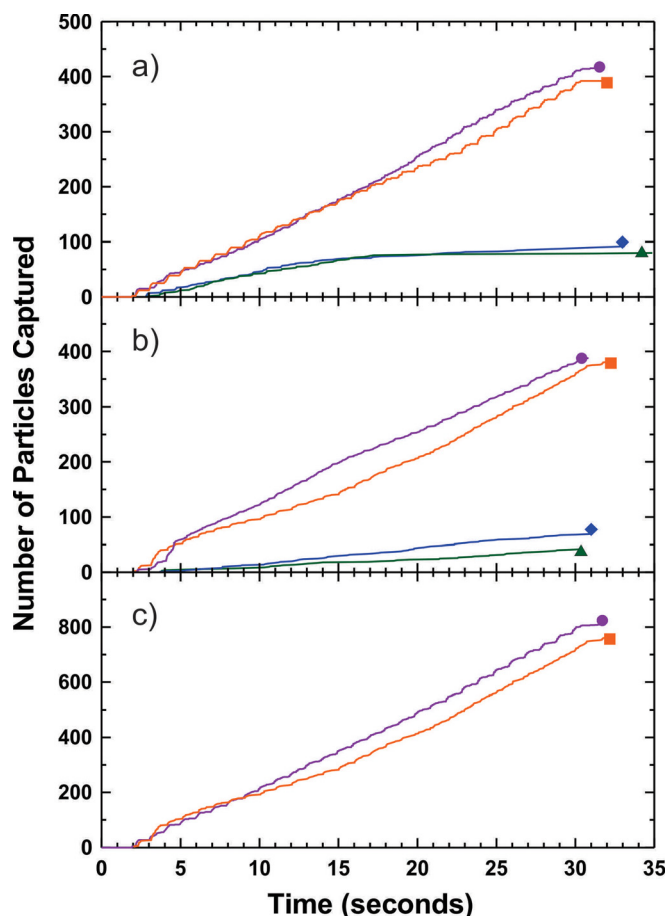


FIG. 6. (a) Number of particles detected as a function of time when the cantilevers were positioned in slots 2 (blue  $\blacklozenge$ ) and 8 (green  $\blacktriangle$ ). Number of particles detected as a function of time with the two-cantilever flow diverter when the cantilevers were positioned in slots 2 (purple  $\bullet$ ) and 8 (orange  $\blacksquare$ ). (b) Number of particles detected as a function of time when the cantilevers were positioned in slots 4 (blue  $\blacklozenge$ ) and 6 (green  $\blacktriangle$ ). Number of particles detected as a function of time with the two-cantilever flow diverter when the cantilevers were positioned in slots 4 (purple  $\bullet$ ) and 6 (orange  $\blacksquare$ ). (c) Total number of particles collected as a function of time using the two-cantilever flow diverter with the cantilevers positioned in slots 2 and 8 (purple  $\bullet$ ) and slots 4 and 6 (orange  $\blacksquare$ ).

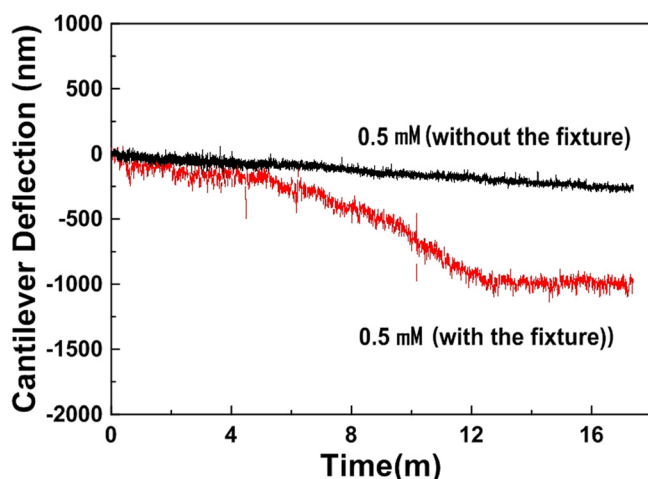


FIG. 7. Cantilever deflection versus time as a result of DNA hybridization for cantilevers positioned in slots 4 and 6 without the flow diverter (black curve) and with the flow diverter (red curve).

flow diverter. It is clear from Figure 7 that influencing the motion of the target molecules to flow directly over the active cantilever can seriously increase the detection rate of cantilever sensors. The experiments shown in Figure 7 were repeated several times with the position of the reference and active cantilevers interchanged with similar results.

## DISCUSSION

Understanding the flow of target particles inside the sensor cell is critical for obtaining accurate and reproducible cantilever sensor measurements. The simulations conducted show that for a geometry as described herein, with one particle inlet, one particle outlet and eight cantilevers arranged around a ring, the exposure of the cantilevers to the target molecules is non-uniform. As a result, in order to perform comparative measurements, the signals from each cantilever must be scaled. Simulations have also shown that a significant improvement can be obtained in terms of both total number of particles detected and the rate of detection when the sensor cell is modified with a large inverted cone placed centrally within the main cylinder of the cell. Although the presence of a large cone somewhat reduced the dispersion in the total number of particles detected by each cantilever, this scenario still requires a calibration scheme. It may be possible to calibrate such a system by performing a controlled experiment where each cantilever in the sensor cell was functionalized to be receptive to the same target particle. Introducing those target particles into the sensor cell would give cantilever deflections, which are proportional to the exposure of the target particles to each cantilever. In such a scenario, it should not be necessary to use a reference cantilever since any additional deflections not due to the detection of the target particles (thermal or vibrational noise) should be the same for each cantilever. If the portion of the cantilever deflections not due to the detection of the target particles is less than 10% of the active signal the effect on the relative ratios should be well within experimental errors.

The best results were obtained when the two-cantilever fixture was used. In this case, the solution carrying the target particles was observed to more directly interact with the cantilevers causing a significant increase in the number of particles detection. One of the most interesting results was the fact that the number of particles detected using the two-cantilever fixture was indifferent to the position of the cantilevers with respect to the particle outlet. The effects of the two-cantilever flow diverter were validated experimentally by performing DNA hybridization experiments with and without the fixture while the cantilevers were in the least sensitive positions (slots 4 and 6). The presence of the fixture increased the cantilever deflection by 4 compared to the signal obtained without the fixture. While it is generally difficult at best to precisely relate the number of particles captured to cantilever deflection, it is reasonable to expect the same order of magnitude change in cantilever deflection and particle count in cantilever sensor measurements. With this in mind, the 8-fold increase in particle count that we observed in simulation is consistent with the 4-fold increase

in cantilever deflection. While our experiments are not designed to probe all aspects of the model, such as the details of the non-uniformity of the flow, they do verify the relative effectiveness of the cantilevers in catching particles.

Although the simulation results presented in this work are semi-quantitative due to the magnitude of the van der Waals force used to describe the interaction between the cantilevers and the target molecules, they provide a reasonably accurate prediction of the relative effectiveness of different cantilevers within the cell and also provide an indication of how actual cantilever deflections will change in response to altering cell geometry. Moreover, the data emphasize the importance of understanding the motion of the target particles through the cantilever sensor cell. In particular, due to the sensitive nature of cantilever sensors and the tendency of small fluid systems to experience laminar flow, it is critical to understand how the target particles are presented to the cantilevers inside the sensor cell. For the case of the geometry presented herein, obtaining the distribution of particles detected by each cantilever is imperative for obtaining reliable and reproducible measurements. This is of even greater importance when multiple cantilevers within the same cell are used at the same time.

## ACKNOWLEDGMENTS

The authors would like to acknowledge NSERC, ACEnet, CFI, and Memorial University for providing partial support of this work. The authors would also like to thank Dr. Iakov Afanassiev and Dr. Alejandro Allievi for useful discussions. A.A. would like to thank the Ministry of Higher Education, Kingdom of Saudi Arabia for scholarship support.

<sup>1</sup>J. R. Barnes, R. J. Stephenson, M. E. Welland, Ch. Gerber, and J. K. Gimzewski, *Nature* **372**, 79–81 (1994).

<sup>2</sup>S. Cherian and T. Thundat, *Appl. Phys. Lett.* **80**, 2219–2221 (2002).

<sup>3</sup>N. Backmann, C. Zahnd, F. Huber, A. Bietsch, A. Plückthun, H. P. Lang, H.-J. Güntherodt, M. Hegner, and Ch. Gerber, *Proc. Natl. Acad. Sci. U.S.A.* **102**, 14587–14592 (2005).

<sup>4</sup>J. Fritz, M. K. Baller, H. P. Lang, H. Rothuizen, P. Vettiger, E. Meyer, H.-J. Güntherodt, Ch. Gerber, and J. K. Gimzewski, *Science* **288**, 316 (2000).

<sup>5</sup>G. Y. Chen, T. Thundat, E. A. Wachter, and R. J. Warmack, *J. Appl. Phys.* **77**, 3618–3622 (1995).

<sup>6</sup>R. Raiteri, G. Nelles, H. J. Butt, W. Knoll, and P. Skladal, *Sens. Actuators B* **61**, 213–217 (1999).

<sup>7</sup>D. Yi, A. Greve, J. H. Hales, L. R. Senesac, D. M. Nicholson, A. Boisen, and T. Thundat, *Appl. Phys. Lett.* **93**, 154102 (2008).

<sup>8</sup>G. H. Wu, R. H. Datar, K. M. Hansen, T. Thundat, R. J. Cote, and A. Majumdar, *Nat. Biotechnol.* **19**, 856–860 (2001).

<sup>9</sup>C. Grogan, R. Raiteri, G. O'Connor, T. Glynn, V. Cunningham, M. Kane, M. Charlton, and D. Leech, *Biosens. Bioelectron.* **17**, 201–220 (2002).

<sup>10</sup>A. Gupta, D. Akin, and R. Bashir, *Appl. Phys. Lett.* **84**, 1976–1978 (2004).

<sup>11</sup>J. Fritz, “Cantilever biosensors,” *Analyst* **133**, 855–863 (2008).

<sup>12</sup>K. M. Goeders, J. S. Colton, and L. A. Bottomley, *Chem. Rev.* **108**, 522–542 (2008).

<sup>13</sup>S. K. Vashist, *AZojono* **3**, 1–15 (2007).

<sup>14</sup>B. Llic, Y. Yang, and H. G. Craighead, *Appl. Phys. Lett.* **85**, 2604–2606 (2004).

<sup>15</sup>O. Hayden, R. Bindeus, C. Haderspöck, K.-J. Mann, B. Wirl, and F. L. Dickert, *Sens. Actuators B* **91**, 316–319 (2003).

<sup>16</sup>T. Tatsuma, Y. Watanabe, N. Oyama, K. Kitakizaki, and M. Haba, *Anal. Chem.* **71**, 3632–3636 (1999).

<sup>17</sup>H. Anderson, M. Jönsson, L. Vestling, U. Lindberg, and T. Aastrup, *Sens. Actuators B* **123**, 27–34 (2007).

<sup>18</sup>M. Jönsson, H. Anderson, U. Lindberg, and T. Aastrup, *Sens. Actuators B* **123**, 21–26 (2007).

<sup>19</sup>C. Köblinger, E. Uttenhalter, S. Drost, F. Aberl, H. Wolf, G. Brink, A. Stanglmaier, and E. Sackmann, *Sens. Actuators B* **24**, 107–112 (1995).

<sup>20</sup>E. Reimhult, C. Larsson, B. Kasemo, and F. Höök, *Anal. Chem.* **76**, 7211–7220 (2004).

<sup>21</sup>T. Viitala, H. Liang, M. Gupta, T. Zwinger, M. Yliperttula, and A. Bunker, *J. Colloid Interface Sci.* **378**, 251–259 (2012).

<sup>22</sup>J. Lammertyn, P. Verboven, E. A. Veraverbeke, S. Vermeir, J. Irudayaraj, and B. M. Nicolai, *Sens. Actuators B* **114**, 728–736 (2006).

<sup>23</sup>A. Cimorelli and J. Luban, *J. Virol.* **74**, 6734–6740 (2000).

<sup>24</sup>J. P. Brody, P. Yager, R. E. Glodstein, and R. H. Austin, *Biophys. J.* **71**, 3430–3441 (1996).

<sup>25</sup>J. Israelachvili, *Intermolecular and Surface Forces*, 3 ed. (Academic Press, 2011).

<sup>26</sup>R. Mckendry, J. Zhang, Y. Arnts, T. Strunz, M. Hegner, H. P. Lang, *Proc. Natl. Acad. Sci. U.S.A.* **99**, 9783–9788 (2002).

<sup>27</sup>K. Castelino, B. Kannan, and A. Majumdar, *Langmuir* **21**, 1956–1961 (2005).

<sup>28</sup>T. Herne and M. Tarlov, *J. Am. Chem. Soc.* **119**, 8916–8920 (1997).

<sup>29</sup>T. Squires, R. Messinger, and S. Manalis, *Nature Biotechnol.* **26**, 417–426 (2008).

<sup>30</sup>J. P. Holman, *Heat Transfer* (McGraw-Hill, 2002).